Calorimeter Heat Flux Trends in NASA's Subscale Rotating Detonation Rocket Engine

Joseph Hernandez-McCloskey*†, Seth A. Reutlinger*, and Daniel I. Pineda‡
The University of Texas at San Antonio (UTSA), San Antonio, Texas, 78249

Thomas W. Teasley§, Dillon M. Petty¶
NASA Marshall Space Flight Center, Huntsville, AL 35812

A calorimeter-style rotating detonation rocket engine (RDRE) outer chamber body was designed, additively manufactured in GRCop-42, and hot-fire tested in test cell 105 at NASA Marshall Space Flight Center (MSFC) in Huntsville, AL in August 2024. Steady-state, spatially resolved heat flux and chamber pressure were measured at 13 and 9 locations from the injector face, respectively, for a variety of test conditions and hardware configurations with gaseous methane and oxygen propellants. The 2-in. diameter highly-instrumented design, enabled by metal additive manufacturing (AM), allowed for simultaneous measurement of heat flux and chamber pressure through 44 long duration hot-fire tests without failure. Of the 44 tests, only 3 of the tests featured chamber pressures below 100 psia and are discussed in this work. Heat flux trends for this subscale hardware are explored with respect to local propellant mass flux for several different injectors, chamber lengths, and chamber "subsonic" area ratios (contraction ratios). Results show that for increasing chamber pressure, a reduced amount of energy per kilogram of propellant is transferred to the wall. Switching injectors affects the near-face heat flux and chamber pressure profiles. Chamber length does not noticeably affect the heat flux profile but increases bulk heat load. A subsonic area ratio greater than 1 reduces heat losses to the wall compared to a straight annulus case. Equivalence ratio shift did not significantly affect heat flux. Computational fluid dynamics (CFD) and conjugate heat transfer (CHT) analyses were performed to delineate 3-D heat transfer and coolant mass flow maldistribution effects and create a calorimeter transfer function to transform heat flux data and mitigate the profile distortions. Additional CFD/CHT simulations were performed using experimental data as boundary conditions to assess local nucleate boiling propensity during testing and to assess projected hot wall temperatures for future fatigue assessment. Vapor fractions were observed locally for several cases. It is anticipated that this effort will provide a common framework for coolant system design/analysis in calorimeter systems for rocket-based and air-breathing combustors, ensuring greater repeatability in calorimetry measurements across the research community.

I. Nomenclature

q''	=	heat flux [MW/m^2]
$\dot{Q}$	=	heat load [MW]
x	=	distance from injector face [in.]
L	=	combustor length [in.]
L'	=	face-to-throat length [in.]
P	=	pressure
T	=	temperature
ϕ	=	equivalence ratio

*Graduate Research Assistant, Department of Mechanical, Aerospace, and Industrial Engineering, AIAA Student Member
†NASA Space Technology Graduate Research Opportunities (NSTGRO) Fellow, Engine Components and Technology Branch
‡Assistant Professor, Department of Mechanical, Aerospace, and Industrial Engineering, AIAA Member
§Lead Combustion Devices Engineer, Engine Components Development & Technology Branch, NASA MSFC, AIAA Member
¶Combustion Devices Engineer, Engine Components Development & Technology Branch, NASA MSFC, AIAA Member

II. Introduction

Liquid rocket engine (LRE) technologies which operate on the deflagrative mode of combustion have approached the limits of the Brayton cycle. With recent combustion performances (i.e., c^*) reaching >99% of the theoretical limit in these architectures, detonation-based combustion presents a promising path to overcome these thermodynamic limitations via a lower-entropy, detonative combustion process. With lower entropy generation across a detonation wave, higher temperatures and pressures can theoretically be achieved for the same reactant mass flux as a deflagrative process [1], which translates into a larger payload capacity via more efficient use of the propellant's chemical energy. Rotating detonation rocket engines (RDREs) are a promising implementation of detonation-based combustion; they feature an annular chamber geometry that allows detonation waves to be self-sustaining, traversing at frequencies on the order of 1–40 kHz at steady-state conditions [2].

Despite their potential for enhancing access to space, the currently unsolved thermal environment of RDREs confines the technology readiness level (TRL) to ground-test only. With the more extreme conditions generated by the unsteady, periodic detonation waves than the (ideally) mode-free operation of a deflagrative combustor, heat transfer to the chamber walls is not well characterized [3]. In deflagrative combustors, the traditional Bartz correlation [4] (or other Nusselt correlations) is typically used to estimate chamber heat flux profiles for the design of active cooling systems [5]; however, the underlying assumptions for such methods do not apply for detonation-based combustors, as the heat transfer mechanisms are different. Without sufficient experimental data to resolve detonative heat flux, an optimal or flight-ready design cannot be realized. In this paper, we discuss the design, analysis, and hot-fire test of a subscale, additively manufactured, calorimeter RDRE chamber for the determination of first-order experimental heat flux trends using simultaneous axial heat load measurements and chamber pressure measurements.

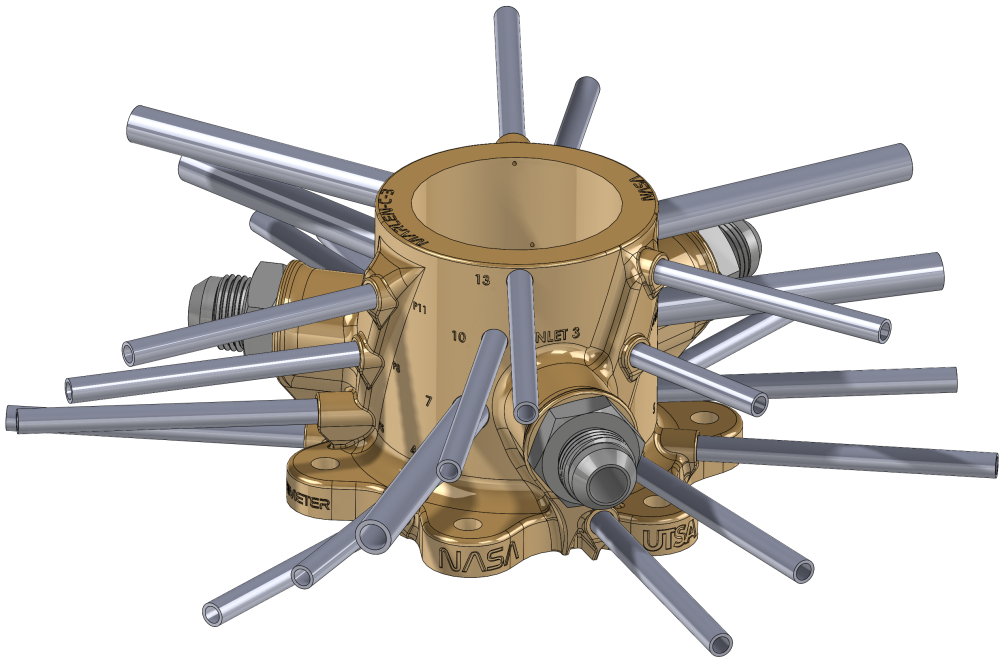

Fig. 1 CAD of calorimeter RDRE outer body fully assembled.

III. Methods

A. Thermal Measurement Approach

Typical implementations of laboratory-scale RDREs use heat-sink hardware (heavy, thermally-conductive hardware with short-duration fires), with recent advancements toward additively manufactured (AM) hardware cooled via axially-oriented channels emerging. Though several robust datasets have been acquired through local conduction analysis in heat-sink hardware [6, 7], heat-sink chamber components are typically limited to <1 second duration hot fires, making connection between steady-state wave dynamics and embedded thermocouple-based heat load difficult.

Optical approaches to heat flux measurement in RDEs/RDREs have been successful and provide valuable information on both flow-field characteristics and heat flux by using image intensity with the velocity-compensation method [8, 9]. Though powerful, these methods are also only limited to short-duration hot-fire tests, as the optically-accessible outer chamber body is uncooled; thus, long-duration trends cannot be fully ascertained, the understanding of which are critical for flight-ready designs.

With actively-cooled axial channel hardware, overall heat loads (and thus bulk heat flux) can be assessed for many conditions using bulk inlet and outlet temperatures to calculate coolant enthalpy difference and thus overall heat load. This enables bulk heat load/heat flux relationships to be determined for overall trend analysis with different hardware configurations and propellant conditions [10, 11]. While overall heat load from a single inlet/outlet coolant measurement enables first-order coolant channel design with new hardware (i.e., expected coolant temperature rise), local hot-wall temperatures cannot be predicted with sufficient accuracy. As local detonative heat flux is anticipated to significantly vary as a function of chamber axial coordinate, local hot-wall temperatures may far exceed those expected from bulk heat flux analysis, leading to potential hardware burn-through. Axially-cooled hardware with heavy instrumentation for local heat flux determination is explored as a resolution to this [12], but the significant burden of sensor packaging within a small footprint limits achievable heat flux axial resolution. Furthermore, the hot-wall thickness required for robust heat flux measurement with thermocouples (must create an ideal conduction region) imposes propellant mass flux limitations due to higher hot-wall temperatures.

For RDRE hardware to achieve a flight-ready TRL, the local thermal environment within the hardware must be known and calculable. Calorimeter chambers (circumferential coolant channels) have been used with great success in many heritage hardware development programs [13] (for deflagration-based engines and other combustion devices) to investigate local wall heat loads across a wide variety of conditions. Through mapping out these local wall heat loads—normalized by local hot wall surface area—spatially-resolved heat flux profiles can be obtained as a function of distance from the injector face. These heat flux profiles are imperative for the design of active cooling systems, as hardware thermal environment must be known *a posteriori* to tailor bulk coolant temperature rise and local coolant channel dimensions for an effective, flight-ready propulsion device.

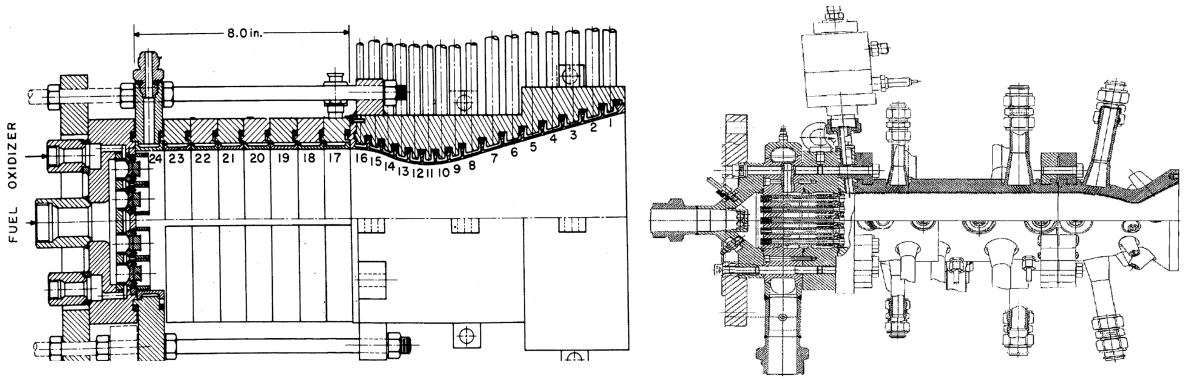

Fig. 2 Calorimeter test hardware for deflagration-based rocket engines, D. R. Bartz [1963] *left* [13], Preclik et al. [1998] *right* [14].

Analysis into RDRE local heat flux via calorimeter hardware has been explored as of 2022 [15], but published data across the community remains extremely sparse. To advance community understanding of these propulsion devices, substantially more data collected via calorimeter hardware is required.

B. Calorimetry

Calorimetry in rocket-based hardware is often performed with water, and local heat load can be assessed through the calorimetry Eqn. 1 below, where $\dot{Q}$ is the heat transfer rate (heat load) [W] transferred through the combustor wall into the coolant, $\dot{m}$ is coolant mass flow rate and Δh is the enthalpy difference between the coolant inlet and outlet. The enthalpy difference is often expressed using $\overline{c_p}$, the average specific heat capacity of water, and $(T_{\text{out}} - T_{\text{in}})$, the temperature rise between the inlet and exit of the coolant station.

$$\dot{Q} = \dot{m}\Delta h \approx \dot{m}\overline{c_p}(T_{\text{out}} - T_{\text{in}}) \tag{1}$$

Assuming total energy transferred into the hot wall is absorbed by the coolant water, heat load $\dot{Q}$ [W] can be normalized by the combustor hot wall surface area A [m^2] to achieve the equivalent heat flux, q'' [MW/m^2] or [BTU/s-in^2], shown in Eqn. 2. When individual circumferential coolant stations are accessible though calorimeter-type hardware, local heat flux may be evaluated by taking the heat absorbed by a local coolant station (with station mass flow rate $\dot{m}_{\text{station}}$) and normalizing that value by the local chamber hot-wall surface area to give local heat flux. Heat flux tabulated as a function of axial combustor coordinate gives insight into local combustion processes.

$$q'' = \frac{\dot{Q}}{A} \tag{2}$$

C. Coolant Channel Design

Owing to the complexities of multiphase fluid dynamics and nonlinearities in boiling heat transfer, many liquid rocket engine coolant systems are designed to suppress coolant boiling. Though enhanced heat transfer offered through nucleate boiling [16, 17]—which arises after a small amount of wall superheat—can be desired for some flight configurations to obtain higher heat transfer rates than mass flow rate/velocity alone can achieve in liquid-only phase, boiling of any kind is not typically desired for calorimetry analysis. To illustrate through the calorimetry equation, coolant bulk temperature rise is the key parameter to evaluate wall heat load $\dot{Q}$ [W]; if the bulk temperature rise is artificially increased via locally enhanced heat transfer rates from nucleate boiling, the calorimetry data will erroneously show a higher heat load than was caused by hot gas effects alone for a given coolant mass flow rate. Thus, to obtain clean calorimetry data—or heat load/heat flux data that shows the effects of the hot gas alone and not coolant phase-change effects—boiling suppression is paramount.

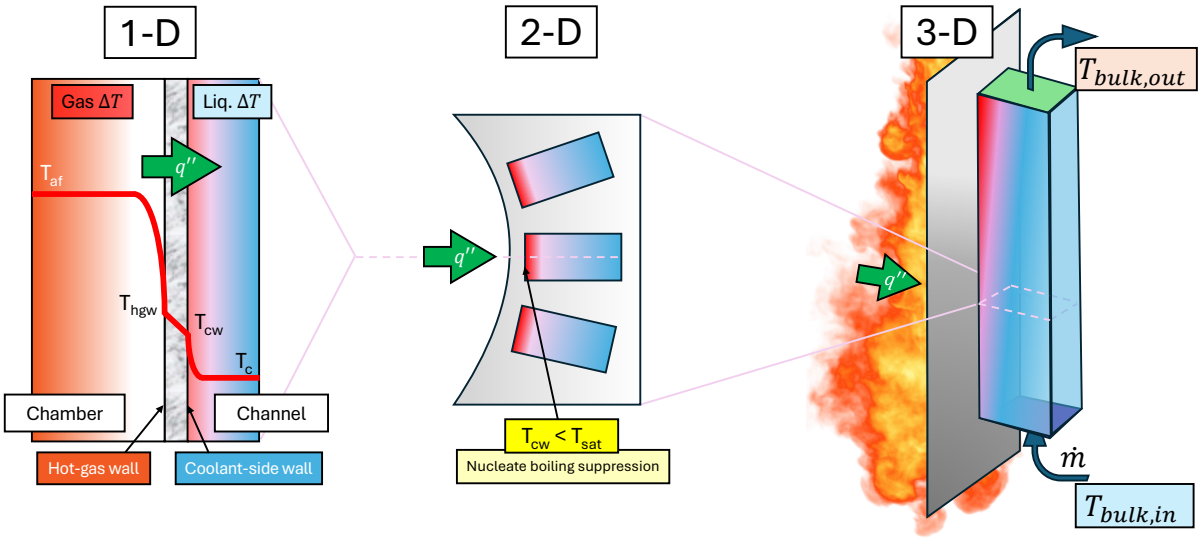

Fig. 3 1-D, 2-D, and 3-D depictions of combustor/coolant channel thermal circuit.

There are two approaches for liquid rocket engine coolant channel design: (1) the burnout heat flux method (q''_{crit}) and (2) the coolant wall film method ($T_{\text{film,crit}}$). While both are generally used in practice, the burnout (critical) heat flux method focuses on keeping the bulk coolant temperature below the saturation temperature (boiling point at a given pressure) to prevent *global* boiling, and the coolant wall film method focuses on keeping the temperature of the coolant wall film, or the interface temperature between the coolant and the chamber-facing coolant channel wall, below the saturation temperature to prevent *local* boiling at the coolant-wall interface. The caveat is that method (1) does not necessarily restrict local nucleate boiling whereas method (2) strictly requires nucleate boiling suppression at all stations. Since local nucleate boiling is not restricted in method (1), then for a minimum channel size (i.e., due to AM process), method (2) requires a higher overall coolant mass flow rate, which also translates to a lower overall coolant temperature rise. By eliminating the possibility of boiling-enhanced heat transfer, calorimetry results can be more readily compared across different conditions/test campaigns.

The primary driver for the calorimeter channel design was method (2), the coolant wall film method, to suppress boiling-enhanced heat transfer effects on the reported heat load data. Since channel minimum dimensions are limited by

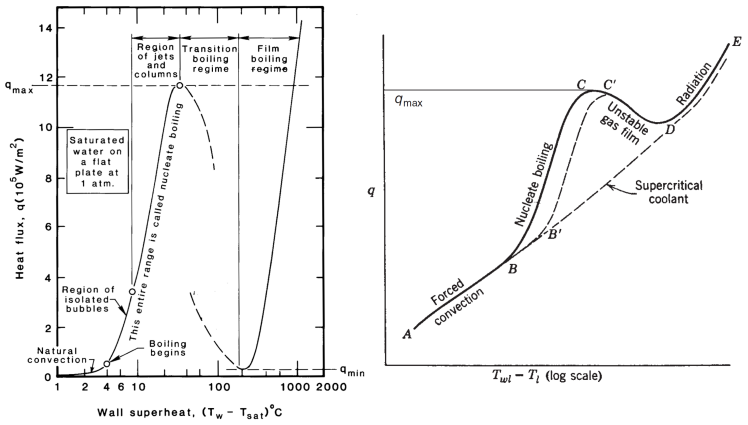

Press. (lbf/in.^{2})	Temp. (°F)
170	368.47
180	373.13
190	377.59
200	381.86
250	401.04
300	417.43
350	431.82
400	444.70
450	456.39
500	467.13
550	477.07
600	486.33
700	503.23
800	518.36
900	532.12
1000	544.75
1100	556.45
1200	567.37
1300	577.60
1400	587.25
1500	596.39

Fig. 4 Boiling heat transfer regimes: [16] *left*, [17] *center*, and coolant water saturation properties [18] *right*.

the L-PBF AM process, channel dimensions were sized to increase probability of successful powder removal, leading to larger-than-ideal cross-sectional areas for subscale hardware cooling. Therefore, mass flow rate was the primary tunable parameter to achieve the required coolant velocity (higher liquid-side heat transfer coefficient, h_{cw}, and thus lower coolant wall temperature) for nucleate boiling suppression. With large channel areas, the mass flow requirement to increase h_{cw} becomes large, which has the effect of driving bulk coolant temperature rise down. This can lead to a low signal-to-noise (SNR) ratio on thermocouple data and can increase error margins on reported heat load data. Thus, the coolant channel sizes were iterated to create a bulk temperature rise of ~40–60°F to balance thermocouple SNR, heat load error margins, and probability of successful powder removal. The resultant coolant mass flow rate (~4.5 lbm/s) was still far above the minimum required for method (1) channel sizing, the burnout heat flux method, and therefore satisfied both boiling suppression criteria. From coolant wall film analysis, the liquid film saturation temperature was desired to be kept below 450°F, which imposed a design back pressure requirement at the exit of the coolant station of about 500 psia, which can be achieved via outlet flow restriction. The equations below are those typically used in this design section [5, 17].

$$q'' = \frac{\dot{Q}}{A} = k\frac{(T_{\mathrm{hgw}} - T_{\mathrm{cw}})}{t_{\mathrm{wall}}} = h_{\mathrm{cw}}(T_{\mathrm{cw}} - T_{\mathrm{c}}) \tag{3}$$

$$h_{\mathrm{cw}} = 0.023\overline{c_p}\frac{\dot{m}_{\mathrm{ch}}}{A_{\mathrm{ch}}}\left(\frac{\rho v D_h}{\mu}\right)^{-0.2}\left(\frac{\mu\overline{c_p}}{\kappa}\right)^{-2/3} \tag{4}$$

D. Calorimeter Hardware Design

The RDRE outer body hardware employs a traditional calorimeter-style design, i.e., with circumferential channels. The 3-in. length hardware features 18 coolant loops that form 13 independently flowing stations for heat transfer measurement. At each coolant station water flow enters the loop, splits in two directions (split branches), then meets at the exit 180-degrees apart from the inlet. The inlet (and corresponding exit) locations for each station are staggered in the azimuthal direction to avoid biasing the hot wall temperature on large zones of the combustor.

The first 6 stations are single-channel loops to allow for fine-resolution heat flux measurement around the forecasted detonation region. Two throat locations also feature a single-channel loop to allow for fine-resolution measurement of throat heat flux for both 2-in. and 3-in. length inner body hardware. The remainder of the coolant stations are dual-channel loops, which report the average heat flux over two axial channel stations to reduce the burden on manufacturing and instrumentation. At each station, flow passageways were filleted to mitigate entrance/exit losses, and coolant loop inlet/outlet areas were sized to be greater than combined split branch areas to mitigate unnecessary restrictions (i.e., pressure losses) and to ensure flow velocities in each split branch reached design values. Lastly, 3 inlet manifolds feed 6 coolant loops each. Common manifolds were implemented to enable coolant water inlet from 3x AS5202-08 fittings with a small footprint on the outer chamber surface, as most of the outer surface real estate was already taken up by fluid outlets and chamber pressure measurement locations. Fig. 5 below shows the fluid volume for the internal passageways within the combustor and the mapping of manifolds to channels.

MANIFOLD 1	
Station #	Channel #
1	1
4	4
7	7
7	8
10	13
13	18

MANIFOLD 2	
Station #	Channel #
2	2
5	5
8	9
8	10
11	14
11	15

MANIFOLD 3	
Station #	Channel #
3	3
6	6
9	11
9	12
12	16
12	17

Fig. 5 Internal fluid volume of calorimeter RDRE showing independent stations.

As the RDRE calorimeter experiments explored in the literature were unable to resolve both in-situ chamber pressure (P_c) and wall heat flux simultaneously, capillary tube attenuated pressure (CTAP) measurements were desired. This design uniquely allows chamber pressure measurement locations at each of the 13 coolant stations to resolve both heat flux and P_c profiles in the same test for correlation development. The MARLEN C-2 version was the primary chamber in the test campaign with 13 coolant stations and 9 CTAP locations, whereas MARLEN C-1 version had 13 coolant stations and 3 CTAP locations (injector face and two throat locations) and was on reserve for backup. The MARLEN C-3 version—pictured in Fig. 9 with 13 coolant stations and 13 CTAP locations—was not manufactured due to schedule.

Following coolant system calculations and CAD model development, computational simulations were performed to analyze local coolant flow velocities, pressure drops, coolant bulk/film temperatures, and resultant combustor wall temperatures. The conjugate heat transfer (CHT) simulations were performed in SolidWorks 2024 Flow Simulation for rapid feedback on CAD feature changes with similar fidelity to prior work [12]. The design simulations used two cases: 1) manifold mass flow inlet boundary conditions and pressure outlet conditions of 500 psig, and 2) channel mass flow outlet boundary conditions and manifold pressure inlet conditions of 540 psig. Both cases were included because there was expected to be some amount of mass flow maldistribution between the channels linked to a common feed manifold, despite having a mass flow-regulated manifold inlet condition. Thermal effects were included via zonal, surface heat flux (q'') boundary conditions with solid material (GRCop-42) conductivity activated. The zonal surface heat flux boundary conditions used in the CHT analysis were scaled from experimental, conduction-based heat flux measurements from Micka et al. [7]. Figs. 6 and 7 show the results of the computational fluid dynamics (CFD)/conjugate heat transfer (CHT) analyses for expected chamber operation.

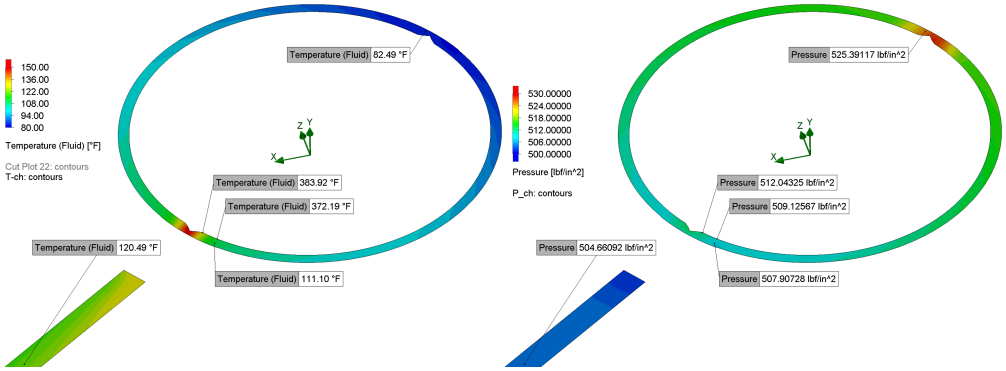

Fig. 6 Coolant pressure drop and bulk/film temperatures from CFD/CHT analysis.

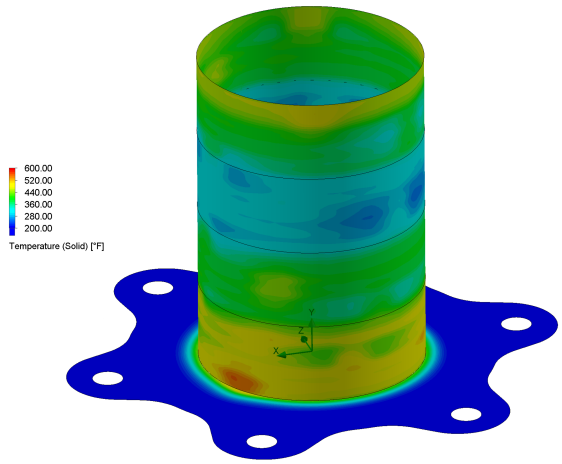

Fig. 7 Combustor wall temperature distribution from CHT analysis.

In the CHT simulations, mass flow rate, temperature, and pressure sensors were placed at the inlet/exit of each circumferential coolant station to monitor mass conservation (continuity) and to obtain bulk enthalpy differences for calculation of resultant heat fluxes. The enthalpy-difference calculation was performed as an analog to the experimental determination of heat fluxes. The resultant heat flux profiles from comparison of simulated enthalpy-difference measurement versus prescribed boundary condition (from scaled data [7]) are shown in Fig. 8, where the effects of both of the coolant flow boundary condition cases are also shown. The stations that straddle two different zonal heat flux boundary conditions are interpolated, leading to the "ramped" shape between the zones.

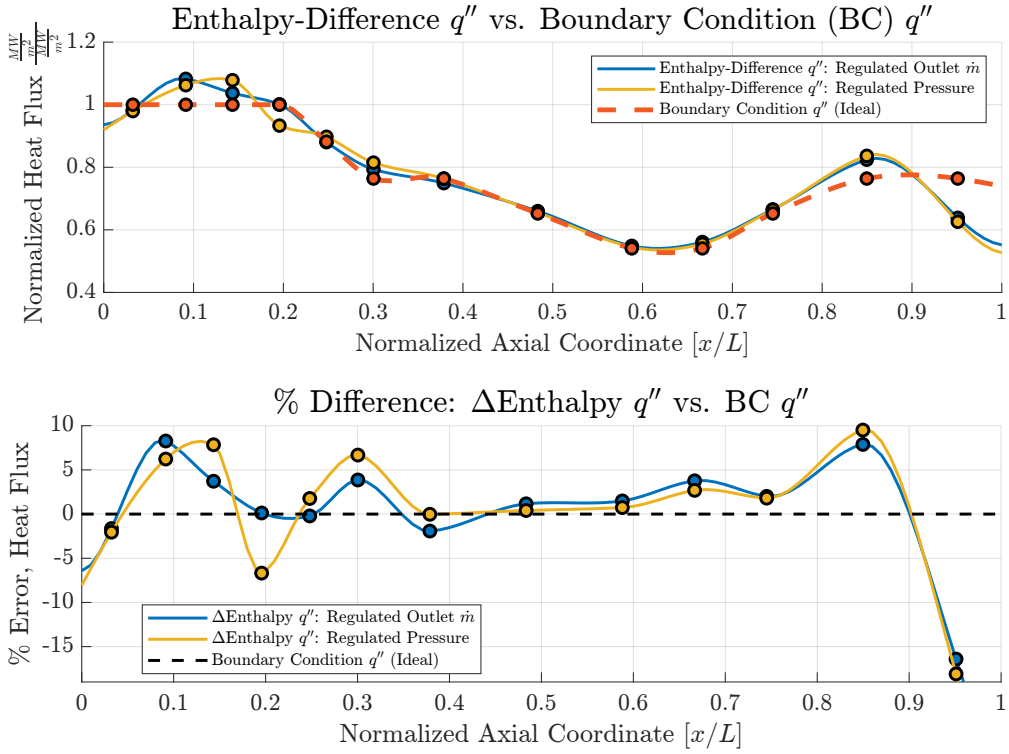

Fig. 8 Applied boundary condition heat flux versus simulation-based enthalpy-difference heat flux.

The effects of geometry, 3-D heat transfer, and mass flow rate maldistribution are shown in Fig. 8. Both outlet pressure-controlled and outlet mass-flow-controlled coolant flow conditions were used to assess heat flux deviations resulting from coolant mass flow distribution or other other effects. Although mass flow maldistribution (pressure-

controlled outlet plot, Fig. 8) does have a pronounced effect in some regions, most of the deviation is from geometry/3-D heat transfer effects that influence the overall amount of energy transferred to the coolant water. For this reason, some sections may absorb more heat than was caused by the hot-wall heat flux alone (over-reporting) or, in the case of the first/last channels, the coolant section is too small relative to the hot wall surface area to report the heat flux effectively (under-reporting). The error between 3-D effects and the 1-D assumption will be discussed in more detail in the results section.

E. Experimental Setup

The calorimeter hardware was manufactured in GRCop-42 via the laser powder bed fusion (L-PBF) process. Two versions of the hardware were printed for risk mitigation. Following powder removal and post-AM hot isostatic pressing (HIP) process, the post-AM machining process was conducted onsite at the East Test Area at MSFC. Hot wall polishing was performed with flapper wheel and isopropyl alcohol (IPA) to create a 16 Ra finish to mitigate roughness-enhanced heat transfer on the combustor hot wall to allow for more direct comparison to other test campaigns. The internal coolant channel surfaces were left rough (no abrasive or chemical smoothing process) to estimate internal roughness as that of the exposed chamber surfaces. Notably, different parameter sets (upskin, downskin, border, etc.) will have different roughness values, but since an extra channel measurement coupon was not printed nor a chamber sectioned via wire-EDM, the outer chamber surface roughness was used as a first-order estimate for these first-order measurements. Prior to tube welding, channels and CTAP thru-holes were inspected for blockages.

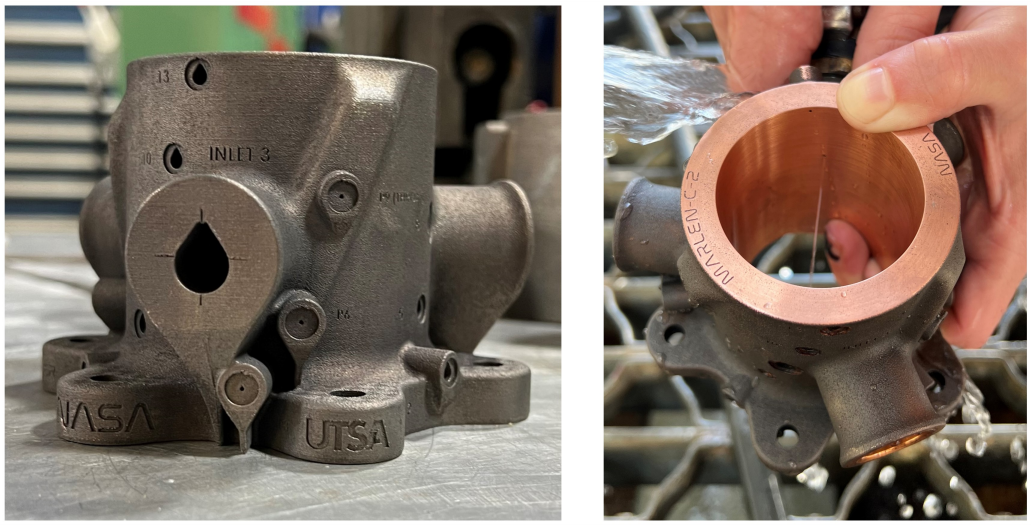

Fig. 9 Additively manufactured calorimeter hardware, as-printed (left), post-AM machined (right).

Once welded, channel resistances were calculated via water flow testing with a turbine flow meter and orifices were sized for target mass flow values. Pressure transducers and thermocouples were installed at the coolant station exit tubes via cross fittings. The orifices were installed into AN unions downstream of the pressure and temperature measurement location. A water blow-down system with a venturi was used to generate the required coolant mass flow rates to both the inner and outer bodies during testing. The nominal water mass flow rate to the outer body was targeted at 4.5 lbm/s (~2 kg/s). Following system characterization, data were collected for 44 tests using gaseous methane and oxygen propellants with a variety of chamber lengths (1-, 1.5-, 2-, 2.5-, 3-in.), contraction ratios or subsonic area ratios [ARs] (1.0, 1.25, 1.5), and injectors (3x).

Lastly, hot fires were conducted for 4–5 seconds on average to allow for coolant water thermocouples to reach steady state temperatures before the shut-down sequence was engaged to conserve propellant for more tests. Fig. 11 shows sample thermocouple data collected from a test and the time at which it was collected.

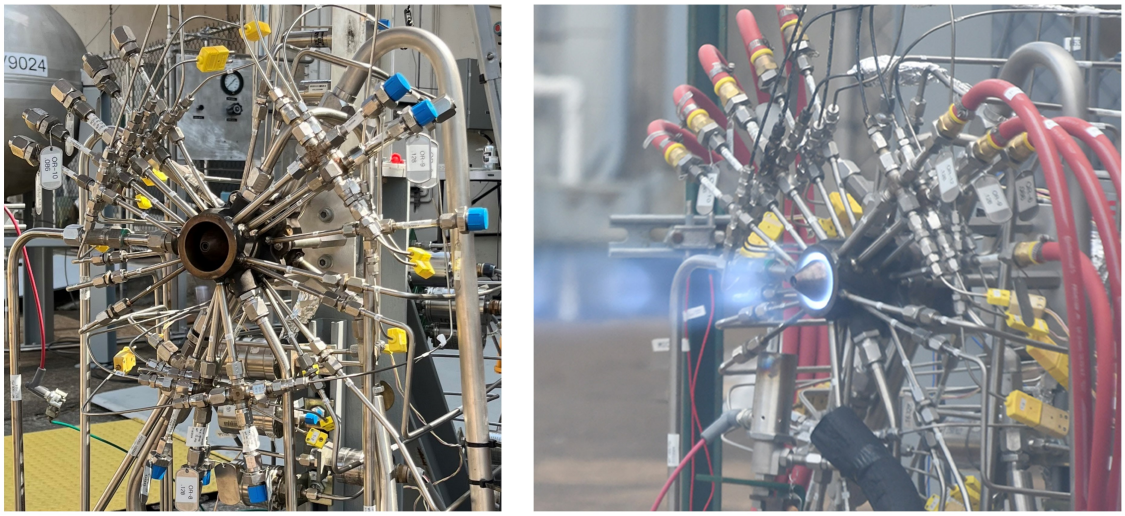

Fig. 10 C-2 Calorimeter during setup (left) and hot fire test (right).

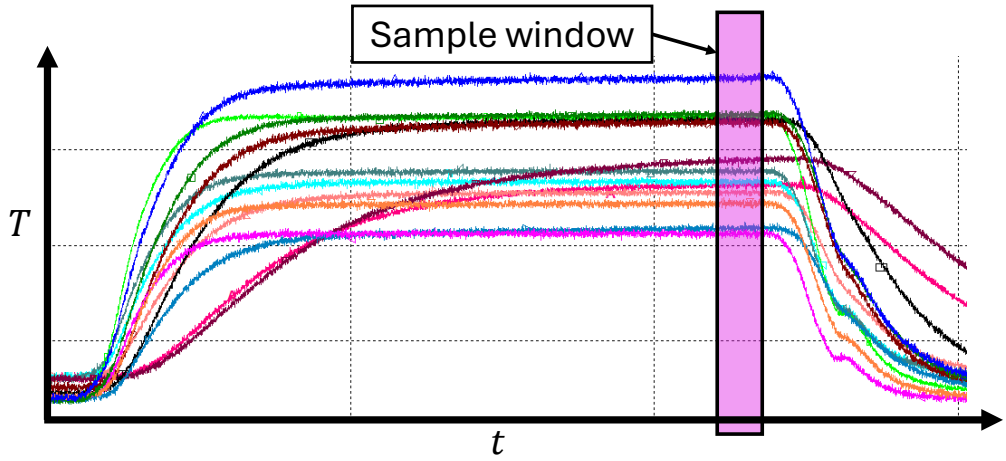

Fig. 11 Thermocouple response during hot fire testing, sampling window for heat load determination.

IV. Results and Analysis

A. Experimental Hot Fire Trends

Due to the limited dataset eligible for analysis in this work (3 data points), bulk load trends as a function of chamber operating condition were not explored. Thus, the analyses in the following subsections focus primarily on comparisons between local heat fluxes and local mass-specific heat (energy) into the wall (local heat flux normalized by local propellant mass flux, [kJ/kg]) for different combustor configurations/conditions. All data is normalized on a scale of 0 to 1, where 1 represents the peak value for a particular plot and remaining data on the plot is scaled accordingly.

The three hot fire tests explored in this work are tests 35, 36, and 42 (T35, T36, T42), where each had chamber pressures below 100 psia. Comparisons are shown between injector types 2 and 3, chamber lengths (L') of 2 in. and 3 in., subsonic area ratios (ARs) of 1.0 and 1.5, and a 3-point equivalence ratio sweep above $\phi = 1$.

1. Overall

Spatially-resolved heat flux and energy transferred into the wall, referred to as specific energy [kJ/kg] in the plots, are shown for the three test cases in Fig. 12. While heat flux profiles provide valuable insight into general trends and are the metric sought to enable first-order coolant system design, the specific energy into wall plot is beneficial for

determining the effects of condition/configuration changes on the energy balance of the system, which ultimately will be utilized in the design of a correlation for obtaining resultant heat flux profiles.

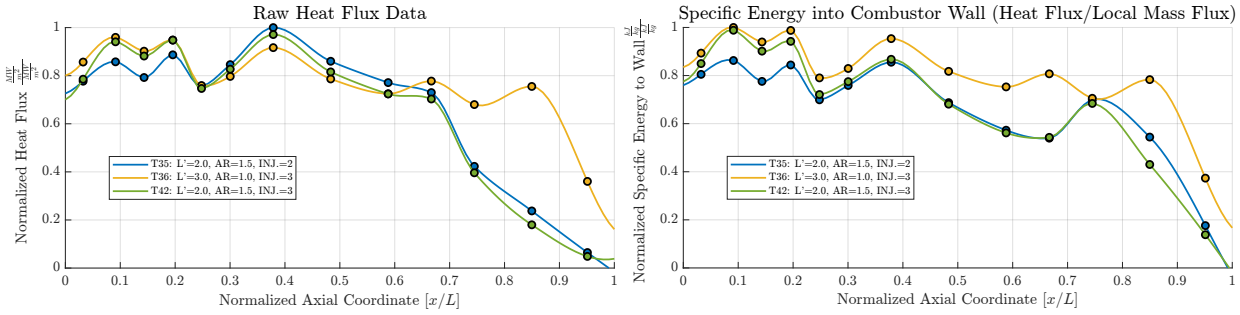

Fig. 12 Overall data: axial profiles for heat flux and (specific) heat loss to wall for cases T35, T36, and T42.

From initial inspection, the raw heat flux profiles had more spatially-varying oscillations than expected. Despite the unexpected oscillatory heat flux profile shapes, lessons learned from the 3-D CHT simulated enthalpy-difference heat flux measurements during the combustor design phase steered the investigation toward the coolant system for further analysis. This analysis is detailed in the section following experimental trends. However, despite the existence of oscillations in the profiles, each station can be reliably compared with itself across different conditions, as each station exhibits a consistent amount of oscillations. The following chamber configuration subsections draw from the above data, each zooming in on different locations or specific cases to determine trends.

2. Injector

The effects of injector change were investigated between T35 and T42 (injectors 2 and 3, respectively). These two tests both had an L' of 2 in., AR of 1.5, and operated at a very similar chamber pressure. The only major perceived difference between the two was the injector swap. Here, the specific energy plot is used rather than the raw heat flux plot to determine trends agnostic to slight deviations in propellant mass flux. In Fig. 13, specific energy into the wall (blue values) are plotted in concert with the local chamber pressure measurements to illustrate injector change effects on both heat losses to the wall and chamber pressure simultaneously.

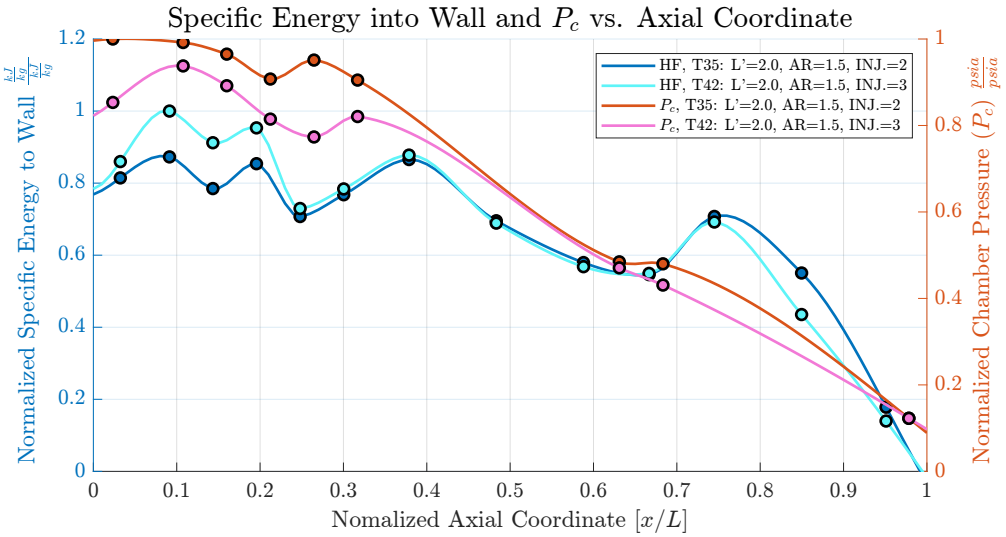

Fig. 13 Injector change effects on wall heat losses and chamber pressure.

In Fig. 13, both injector 2 and injector 3 specific energy data collapse together downstream of the near-injector zone around $x/L = 0.25$ and before the combustor throat around $x/L = 0.65$. Despite their similarity throughout most of the combustor length, there is a marked difference in the near-injector region profile, as injector 3 shows increased energy

into the wall compared to injector 2. Similarly, the P_c data also nearly collapses downstream of the near-injector region around $x/L = 0.4$ and show a pronounced difference near the injector, but the effect is opposite to wall heating, as the chamber pressure is reduced in the near-injector region. These effects are analyzed in more detail through a zoomed-in view in Fig. 14.

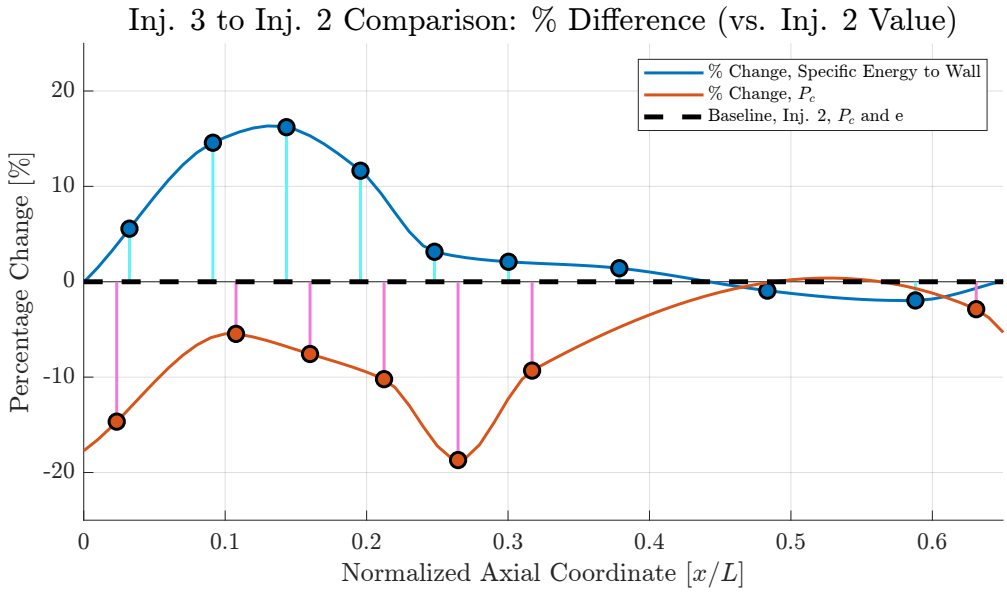

Fig. 14 Comparison of spatially-resolved energy into wall and P_c for injector 3 vs. injector 2 (baseline).

Injector 3 had a higher amount of specific energy into the wall (and heat flux, seen in Fig. 13) in the near-injector region compared to injector 2, but a lower overall P_c in the same region. Interestingly, despite injector 3 having a lower overall P_c magnitude in the near-injector region, an increasing hump in P_c is present that corresponds to an increasing hump in wall heating.

3. Length

In this analysis, T36 (L' = 2 in.) and T42 (L' = 3 in.) are compared as they have the same injector (3). The raw heat flux profiles are plotted rather than wall heat losses due to the chamber AR not being consistent.

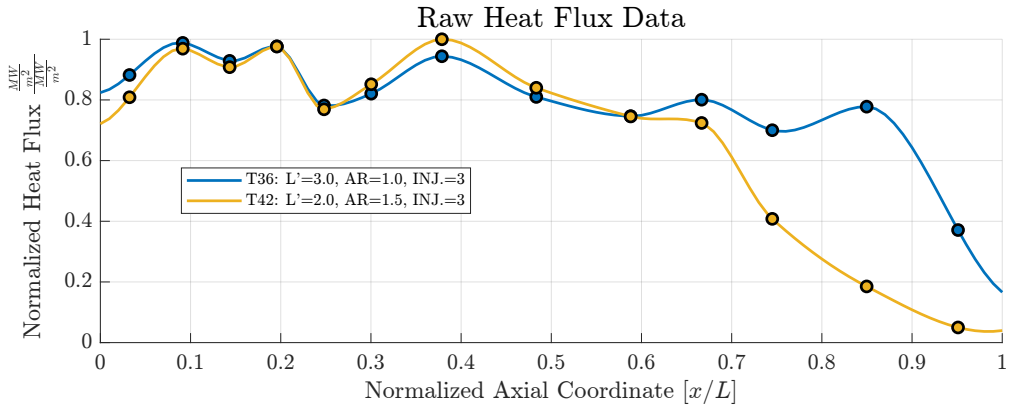

Fig. 15 Heat flux profiles for chamber length comparison, L' = 2 in. vs. L' = 3 in.

From 15, the raw heat flux profiles generally follow the same trend throughout the chamber length up until the 2 in. L' combustor throat. After this point, the lengthier chamber maintains consistent heat flux magnitude further downstream compared to the shorter chamber, as the P_c magnitude remained on a consistent trend in the lengthier

hardware until it reached the 3 in. throat. For the shorter chamber, an earlier throat location in x/L means an earlier expansion of combustion products and lower local heat fluxes in the expanding region when compared with the same x/L in a lengthier chamber. With more chamber hot gas wall surface area available for heating upstream of the throat compared with the shorter chamber length case, a higher overall heat load will result. This effect can be directly calculated by summing the individual station heat loads, which results in lengthier combustors picking up more heat for a given chamber pressure.

4. Area Ratio (AR)

T36 and T42 are compared for chamber subsonic area ratio (AR) trends as they both use the same injector (3). Data is only plotted upstream of the 2 in. L' combustor throat to show the effect of a straight annulus versus the AR 1.5 case only.

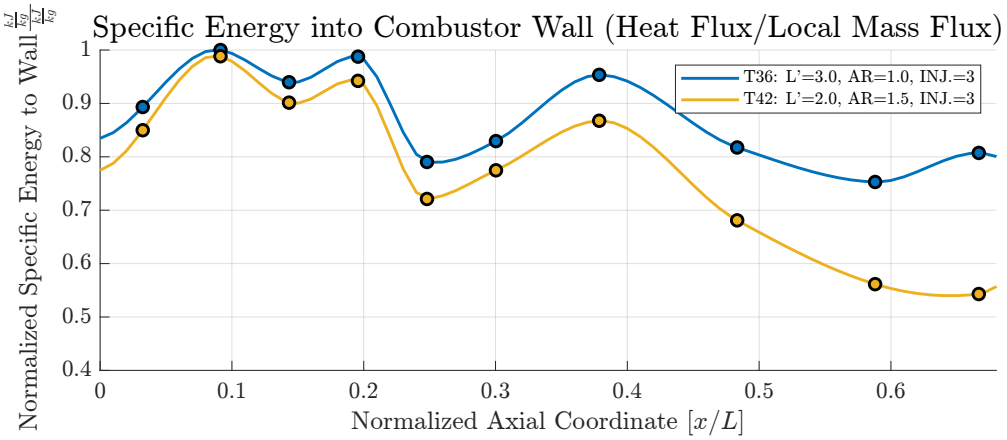

Fig. 16 Specific energy into wall for subsonic area ratio (AR) comparison, AR = 1 vs. AR = 1.5

The AR trend can be visualized in the specific energy plot in Fig. 16. As x/L coordinate increases, the specific energy into the combustor wall diverges, with the increasing AR case resulting in lower heat into the combustor wall. This effect can be seen more closely in Fig. 17, where the AR 1.5 case is plotted against the baseline AR 1.0 case.

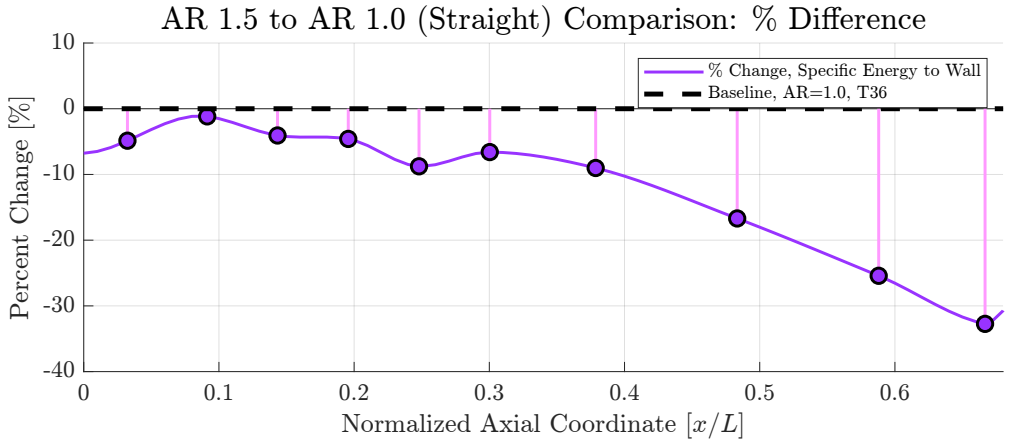

Fig. 17 Comparison of specific energy into wall between AR 1.5 vs. AR 1.0 (baseline)

From this plot, the percentage change in specific energy to the wall is consistently lower than in the straight annulus case. After the near-injector region around $x/L = 0.3$ the percentage change in specific energy to the wall decreases at a consistent rate, whereas the near-injector region, although still negative, appears to be affected some by wave activity, noted by the oscillatory behavior.

5. Equivalence Ratio

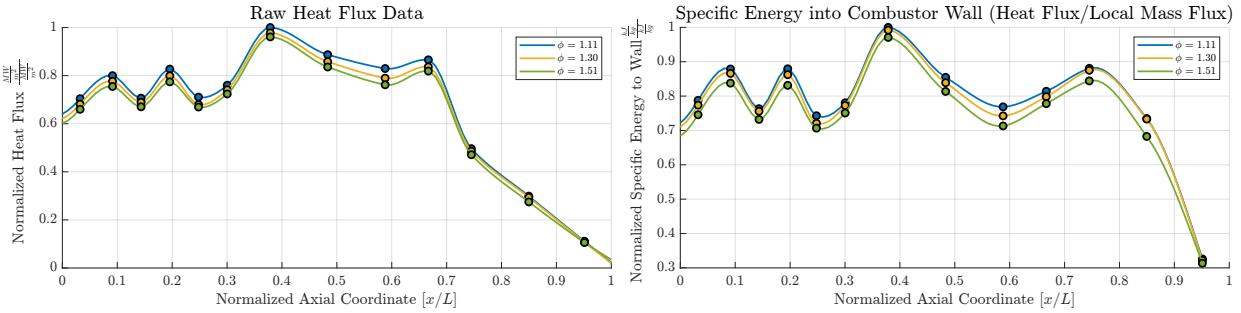

Fig. 18 Equivalence ratio variation effects on heat flux and specific energy into wall.

From Fig. 18, there is a very slight effect of equivalence ratio on heat flux and energy into the combustor wall. Despite the small magnitude of change between conditions, a trend is clearly shown that departing from the stoichiometric condition results in lower heat flux and reduced wall heating. This effect is due to a lower heat release rate occurring within the combustor for a departure from an equivalence ratio of 1. Thus, the decrease in the wall heat flux/wall heating is a direct result of the decrease in hot gas energy content.

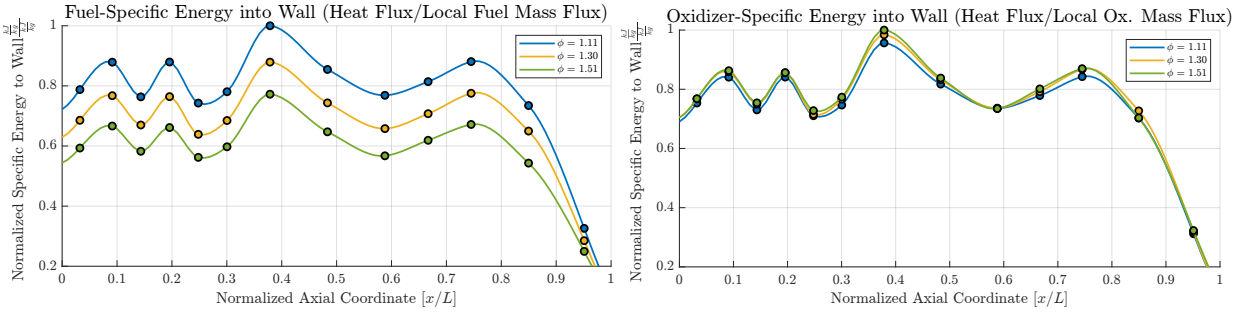

Fig. 19 Fuel-rich equivalence ratios, wall heat loss dependence on fuel mass vs. oxidizer mass.

Since the cases shown in the equivalence ratio sweep occur in the fuel-rich regime (ϕ>1), additional plots were made in Fig. 19 to explore fuel versus oxidizer contribution to the wall heating. The plot on the left in Fig. 19 shows the heat flux normalized by local fuel mass flux (fuel-mass-specific energy into wall) whereas the plot on the right shows heat flux normalized by local oxidizer mass flux (oxidizer-mass-specific energy into wall). It can be seen on the fuel-normalized plot that, for these fuel-rich equivalence ratio cases, an increasing amount of fuel has a pronounced effect on decreasing the wall heating. In contrast, when these same curves are normalized by local oxidizer mass flux, the curves nearly collapse on each other, meaning little effect. Thus, the reduction in wall heating is not caused by the deficient reactant (oxidizer) but by the excess reactant (fuel). Further test cases will be conducted on fuel-lean cases to see if this trend follows on the other size of the equivalence ratio curve (ϕ<1).

6. Modal Shift

Lastly, the effect of wave mode shift was seen in the chamber pressure data and ultimately in the thermocouple data. The periodic P_c oscillation due to wave mode transition corresponds with periodic thermocouple temperature oscillation, meaning there is a clear connection between wave dynamics and heat flux. This trend will be analyzed in future test campaigns.

B. Calorimeter Transfer Function

Although first-order heat flux trends were analyzed for both global and individual axial stations across various test conditions, further insight into the overall oscillatory profile was sought. From the calorimeter design section, propensity for coolant mass flow maldistribution within the hardware was seen. Furthermore, because the exit orifices were sized

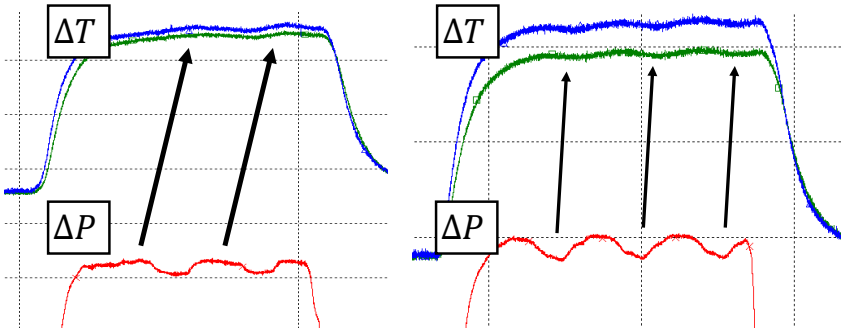

Fig. 20 Wave mode transition effects on thermocouple data.

based on one-at-a-time time measurements rather than all-outlets-at-a-time measurements (for a given inlet manifold), the flow of through each section had robust C_d measurements but were not able to correct the ensemble maldistribution. Thus, it was postulated whether the maldistribution amount, or individual-circuit deviation from ideal, was the same between each test and if a relation could be formed to correct for this. For each test, the total mass flow rate into the calorimeter outer body was summed, then divided by the number of channels (18) to find the ideal single-channel and double-channel flow rates. The percentage error for each circuit flow from ideal is tabulated in Fig. 21, where each of the tests very nearly collapsed.

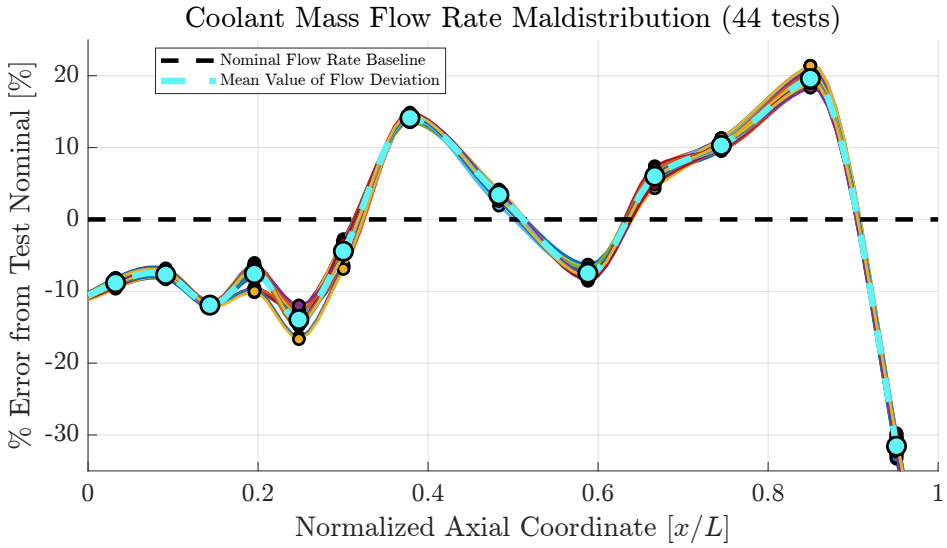

Coolant Mass Flow Deviation	
Station	Mean % Error
1	-8.82%
2	-7.67%
3	-11.93%
4	-7.56%
5	-13.94%
6	-4.42%
7	14.12%
8	3.42%
9	-7.48%
10	6.01%
11	10.30%
12	19.59%
13	-31.56%

Fig. 21 Coolant mass flow rate % error from single-channel/double-channel nominal values.

CHT simulations were performed with the mass flow distribution curve in Fig. 21 to explore the effects of both the actual coolant mass flow maldistribution and 3-D heat transfer/geometry effects simultaneously on resultant enthalpy-difference heat flux measurements. Various heat flux boundary conditions were applied across several simulations to determine how boundary condition heat flux perturbation affects the resultant enthalpy-difference heat flux calculation. The plot in Fig. 22 shows the mean deviation for the enthalpy-difference heat flux versus prescribed boundary condition heat flux for the test cases. The output array of points in Fig. 22 is termed the heat flux deviation vector $\boldsymbol{\zeta}$ (HDV).

From the figure, several stations (like station 7) yielded low sensitivity and maintained a similar enthalpy-difference heat flux output regardless of boundary condition heat flux applied. Other stations which exhibited higher sensitivity (like station 4) were affected more by heat flux gradients versus the constant wall heat flux boundary condition, which encouraged larger heat transfer cross-talk depending on how steep of a heat flux profile was applied. Thus, an intial design of CHT experiments must be conducted to determine how likely some boundary condition heat fluxes would be, as to not skew the HDV too far by unrealistic heat flux gradients. Further details on the HDV training process will be

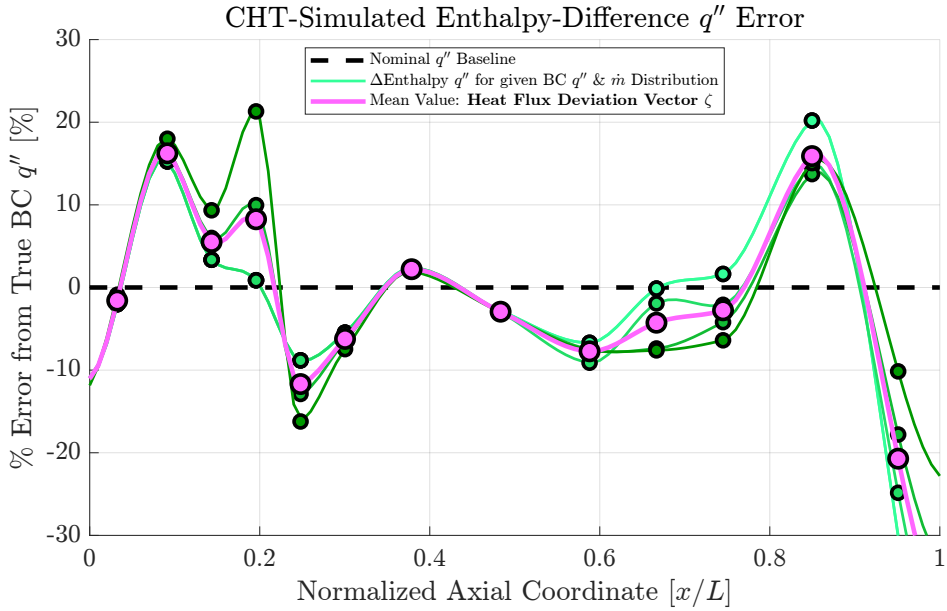

Heat Flux Deviation Vector (ζ)	
Station	Mean % Error
1	-1.58%
2	16.24%
3	5.51%
4	8.26%
5	-11.69%
6	-6.23%
7	2.21%
8	-2.93%
9	-7.72%
10	-4.26%
11	-2.76%
12	15.90%
13	-20.72%

Fig. 22 Resultant enthalpy-difference heat flux response to perturbed BC HF inputs *left*, output heat flux deviation vector (ζ) *right*.

discussed in future work.

The process of transforming the calorimeter data from as-measured heat flux into theoretical heat flux is shown in Eqn. 5. Here, $\boldsymbol{H}_{cal}$ is termed the calorimeter transfer function (CTF), Eqn. 6, which transforms the enthalpy-difference, measured heat flux data $\boldsymbol{q}''_{meas}$ based on the heat flux deviation vector $\boldsymbol{\zeta}$ (HDV) found from 3-D CHT. $\boldsymbol{K}$, Eqn. 7, is a scaling constant to properly scale the calorimeter transfer function to the specific test case and the theoretical $\boldsymbol{q}''_{theo}$ vector represents the probable applied heat flux. $\boldsymbol{H}_{cal}$ in this notation only includes the heat flux deviation vector, as it is a constant inherent to the calorimeter hardware (based on typical coolant mass flow distribution and 3-D heat transfer/geometry effects), whereas the scaling factor is based on the individual conditions analyzed. The equation is expressed in this form to follow conventional notation, however due to the iterative nature of the problem, it may be easier to express this as a simple dot product, Eqn. 8, which is solved iteratively on a component-by-component basis for each coolant station to find $\boldsymbol{q}''_{theo}$.

$$\boldsymbol{q}''_{theo} = (\boldsymbol{H}_{cal} \cdot \boldsymbol{K})\boldsymbol{q}''_{meas} \tag{5}$$

$$\boldsymbol{H}_{cal} = \frac{1}{\boldsymbol{\zeta}} \tag{6}$$

$$\boldsymbol{K} = \left[1 - \frac{\boldsymbol{q}''_{theo}}{\boldsymbol{q}''_{meas}}\right] \tag{7}$$

$$\left(\boldsymbol{q}''_{theo} \cdot \boldsymbol{\zeta}\right) + \boldsymbol{q}''_{theo} = \boldsymbol{q}''_{meas} \tag{8}$$

Examples of transformed heat flux profiles are shown in Fig. 23. Through this analysis, the resultant heat flux profiles can be seen with 3-D effects and coolant maldistribution effects mitigated or removed. These also more closely resemble those seen in the literature [15].

In summary, though mass flow maldistribution effects in the hardware contributed to the oscillatory behavior via the common-feed manifolds (no ability to separately tune both inlets/outlets of individual channels), heat flux errors still existed due to 3-D heat transfer/geometry effects. These geometry effects are postulated to be more extreme with small-scale hardware, as many geometric modifications are made to accommodate instrumentation (i.e., overhanging surfaces on outside of hardware) and make up a larger percentage of the total hardware cross section than they would for a larger chamber diameter. To correct for these errors introduced, a calorimeter transfer function may be constructed for

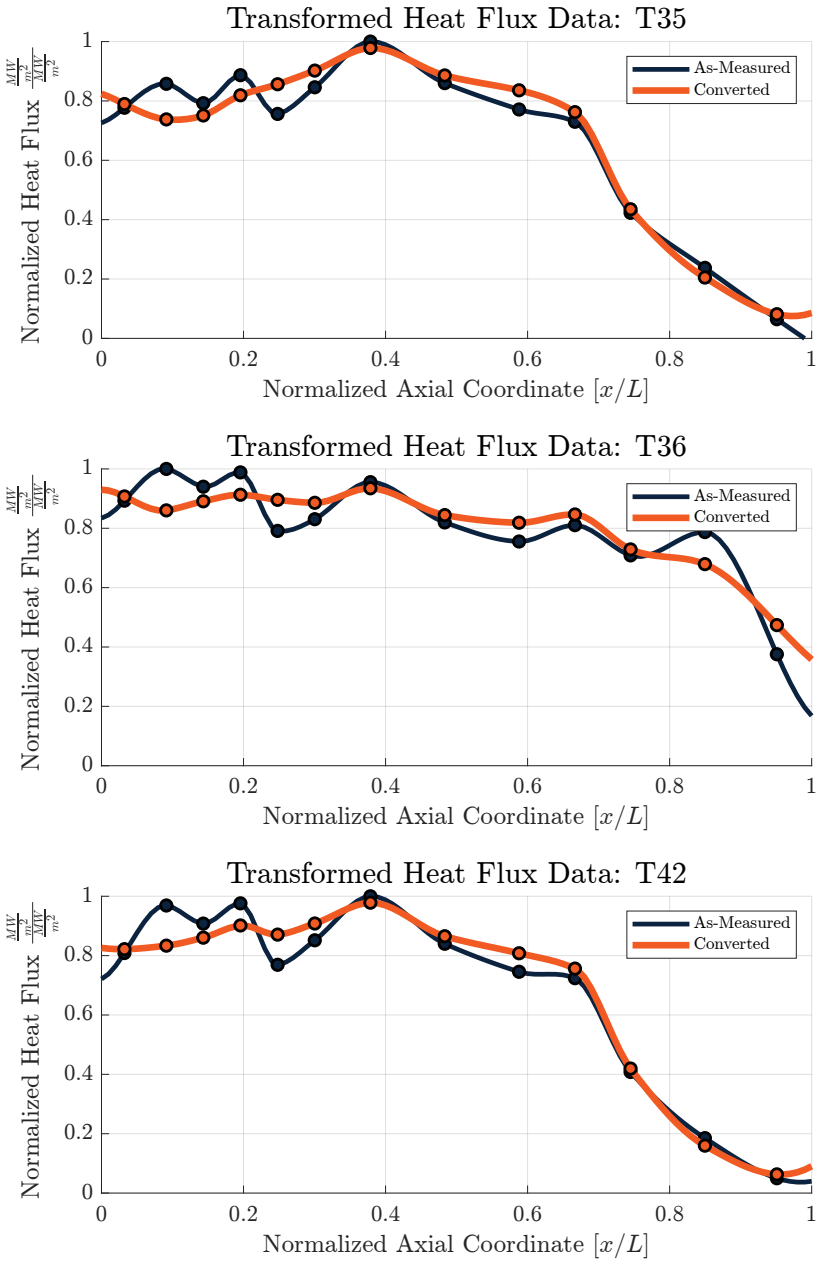

Fig. 23 Transformed heat flux profiles via calorimeter transfer function.

a hardware test configuration to transform recorded enthalpy-difference heat flux data and better compare heat flux profiles across the community with minimum bias from maldistribution or 3-D effects. After conducting this analysis, a literature search revealed that the process developed in this work has similar roots to simulation-based corrections of experimental measurements in generalized calorimetry analyses, including work from the National Institute of Standards and Technology (NIST) [19–21].

C. Conjugate Heat Transfer: Boiling Analysis

Though the CTF process yields results that can be better compared to literature than raw data alone, the heat flux deviation vector here assumes no heat transfer augmentation due to boiling effects. While this should be true in the case of nominal operation of calorimeter hardware, it was found that the orifices used in the test campaign resulted in much lower back pressures than the design values. This resulted in decreased allowable saturation temperature

values of the coolant water. Unfortunately, the heat fluxes and coolant temperature rises were still within the design order-of-magnitude, meaning the coolant wall film was likely near the saturation temperature in several locations, i.e., near the channel exits for many test cases.

To raise suspicions further, an interesting effect occurred during testing, where the coolant pressure would jump slightly (with varying magnitude) during hot fire operation. This was postulated to be related to some amount of vapor formation, as the coolant water was running both well before and throughout the end of the hot fire test and maintained a steady rate of decline (blow-down system) except for during some hot fire operations. In Fig. 24, this pressure jump is shown at station 9 for a "high" heat flux case compared to the pressure profile of a “low” heat flux case (though still high enough to potentially cause local boiling).

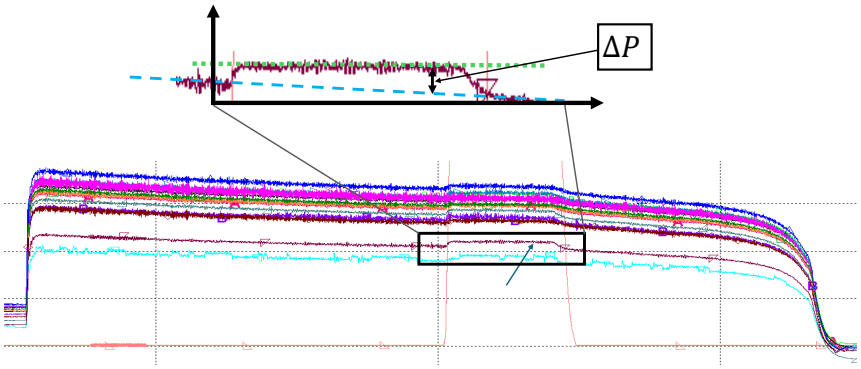

Fig. 24 Coolant pressure jump during onset of large heat flux, potential indicator for some amount of boiling

Though the bulk temperature of the coolant at the exits remained below the local saturation temperature in all cases, it is not inherent from experimental data alone (coolant pressure and temperature) whether localized regions achieved wall superheat and thus nucleate boiling. To further explore this concern, a computational analysis was desired to determine which regions of the channel, if any, achieved locally-enhanced heating.

3-D multiphase conjugate heat transfer analyses were conducted using ANSYS Fluent. Simplified versions of single-channel and double-channel setups were created to simulate the heat transfer into the fluid from an applied heat flux boundary condition at the chamber hot wall. A full 3-D model of the channel was desired (as opposed to a 1-D or 2-D model) to ensure geometry-dependent effects were accounted for in the heat transfer analysis. A sample channel outlet pressure (measured upstream of the exit orifice) from experiment was used as the outlet boundary condition and nominal mass flow rate was used as the inlet boundary condition. The Lee evaporation-condensation mechanism was used as the multiphase model in ANSYS with a user-defined pressure vs. saturation temperature curve for water using the values from table A-3E in Moran et al. [18]. A wall surface roughness of 200 μin was used and typical meshes ranged from 1 million to 20 million elements. Inflation layers were used at the fluid-solid interfaces to capture boundary layers. Temperature contours along the coolant-side wall were plotted along with vapor fractions in Figs. 25 and 26 to assess local wall superheat and presence of boiling.

From the test cases in Figs. 25 and 26 it is clear that local wall superheat, and the presence of vapor fraction, indicate local nucleate boiling toward the channel exits (convergent point between split sections). This is because, for a given station, the bulk coolant temperature is the hottest near the channel exits, meaning the coolant-side wall will also be the hottest near the channel exits for a prescribed heat flux boundary condition. Furthermore, the static pressure at the channel exits is also at its lowest in the station (due to channel pressure drop) leaving the exits exposed to both elevated temperatures and lower allowable saturation temperatures. These conditions enable the onset of nucleate boiling with greater ease.

Since these analyses confirmed presence of vapor for some level of applied boundary condition heat flux, future analyses will be conducted to monitor local coolant-wall film coefficient h_{cw} against degree of wall superheat. Once properties are known locally, estimates for local heat transfer augmentation will be calculated and effects effect on global dT will be explored to determine effects on experimental, enthalpy-difference heat flux.

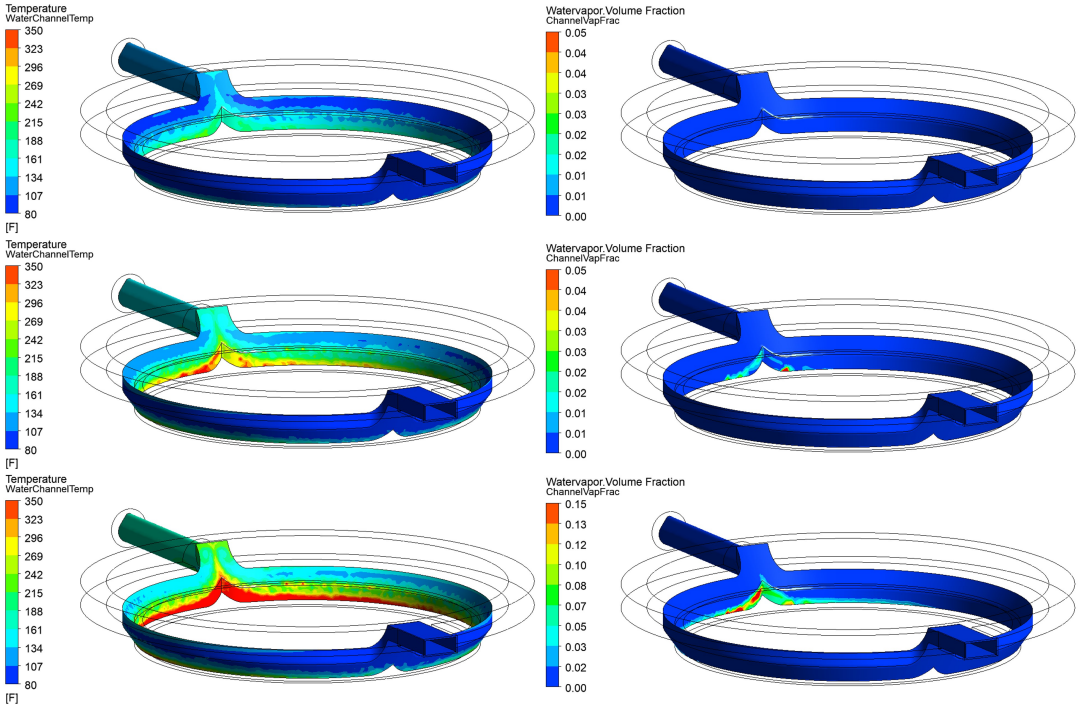

Fig. 25 Single-channel: zones of wall superheat (red) and vapor fraction for arbitrary low-, medium-, and high-heat flux boundary conditions.

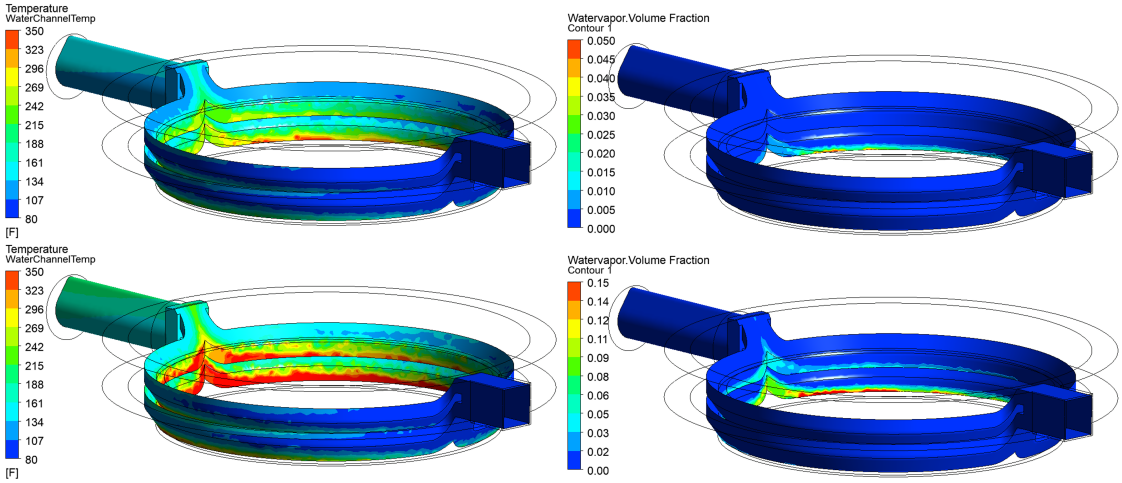

Fig. 26 Double-channel: zones of wall superheat (red) and vapor fraction for arbitrary medium- and high- heat flux boundary conditions.

Summary and Future Work

Simultaneous heat flux and chamber pressure measurements were recorded at NASA Marshall Space Flight Center through the hardware developed in this work. 3 of the 44 hot fire test cases had chamber pressures below 100 psia and could be used for first-order trend analysis. For these cases, the most significant effects on local heat flux and local wall heat losses were related to the injector and the combustor AR, Figs. 14 and 17, where changing the injector affected the near-face heat flux profile and increasing combustor AR reduced wall heat losses for a given local mass flux. The most significant effect on bulk heat load was related to the combustor length, as a longer chamber has more surface area to absorb heat from the hot gas upstream of the throat. Wave mode switching was also shown to have an effect on local

thermocouple temperature variations, though more data is needed to ascertain local heat flux and bulk heat load trends. In future testing, more conditions targeting a broader sweep of equivalence ratio will be sought to verify if the trend shown in Fig. 19 switches for fuel-lean conditions. Further test cases will be sought to determine relationships between wave dynamics and measured heat flux.

The calorimeter transfer function process developed in this work used 3-D CHT simulations to predict deviations in local enthalpy-difference heat flux (measurement) for a series of applied heat flux boundary conditions (true value). Though this process, the oscillatory trends were mitigated in the measured heat flux profiles, enabling greater comparison with literature values with reduced bias from coolant flow maldistribution or 3-D effects. For future calorimeter testing, transfer functions will be developed for each new set of hardware (and/or with different coolant flow conditions), and anticipated heat flux perturbations will be used with 3-D CHT to gather training data for new heat flux deviation vectors.

3-D multiphase CHT analyses on coolant channel geometries confirmed local vapor fractions, thus, nucleate boiling, for given heat fluxes. These analyses confirm trends noted in the pressure data given the decreased allowable coolant saturation temperature per the larger coolant exit orifices used in this test campaign. Though the effects of any potential heat transfer augmentation could not readily be delineated from these analyses, future work will consist of analyzing local film coefficients and local wall superheat to determine boiling effects on both local and overall coolant dT.

From this first-order mapping of local heat flux trends, it is evident that significantly more data is needed to analyze the trends in greater detail. While more conditions will be explored through hot fire test, larger data sets spanning broad conditions, scales, geometries, propellants, etc., are also sought from the propulsion community as we seek to advance the TRL from laboratory test to space flight. Through the design, analysis, and data reduction processes presented, it is anticipated that this work will provide a common foundation to build larger calorimetry datasets within our field.

Acknowledgments

This work was funded by the NASA Space Technology Mission Directorate. J.H-M. is supported by a NASA Space Technology Graduate Research Opportunity (NSTGRO) award, Grant No. 80NSSC22K1215, and S.A.R. is supported in part by AFRL ML-RCP project number POA-24-RQ-010 and The American Chemical Society Petroleum Research Fund Grant No. 65560-DNI6. Additionally, this effort has been supported in part by a NASA MIRO Grant, No. 80NSSC19M0194. The authors would like to acknowledge the instrumental support of the NASA MSFC ET10 test crew, the Dannys, and the weld shop in preparing the calorimeter hardware for testing and hot fire operations. The authors thank ER13 at NASA MSFC for their support of the fabrication and testing effort. The authors thank Ari Goldman and Michaela Hemming for support of data collection activities during the hot fire test campaign.

References

[1] Zel'dovich, Y., "To the Question of Energy Use of Detonation Combustion," *Journal of Propulsion and Power*, Vol. 22, No. 3, 2006, pp. 588–592. https://doi.org/10.2514/1.22705.

[2] Hargus, W. A., Schumaker, S. A., and Paulson, E. J., "Air Force Research Laboratory Rotating Detonation Rocket Engine Development," *2018 Joint Propulsion Conference*, American Institute of Aeronautics and Astronautics, Cincinnati, Ohio, 2018. https://doi.org/10.2514/6.2018-4876, URL https://arc.aiaa.org/doi/10.2514/6.2018-4876.

[3] Teasley, T., Petty, D., Skinner, S., and Hernandez-Mccloskey, J., "NASA'S COMPACT HIGH-EFFICIENCY ROTATING DETONATION ROCKET ENGINE FOR MARS INTERPLANETARY MISSIONS," *6th Annual AAS Guidance, Navigation and Control Conference*, 2024. URL https://ntrs.nasa.gov/citations/20240000933.

[4] Bartz, D. R., "A Simple Equation for Rapid Estimation of Rocket Nozzle Convective Heat Transfer Coefficients," *Journal of Jet Propulsion*, Vol. 27, No. 1, 1957, pp. 49–53. https://doi.org/10.2514/8.12572, URL https://arc.aiaa.org/doi/10.2514/8.12572.

[5] Kirchberger, C., "Investigation on Heat Transfer in Small Hydrocarbon Rocket Combustion Chambers," Ph.D. thesis, 2014.

[6] Lim, D., "EXPERIMENTAL STUDIES OF LIQUID INJECTOR RESPONSE AND WALL HEAT FLUX IN A ROTATING DETONATION ROCKET ENGINE A Dissertation," Ph.D. thesis, Purdue University, 2019.

[7] Micka, D. J., Daines, G. W., Sosa, J., Burke, R., Ahmed, K. A., Bennewitz, J. W., Danczyk, S. A., Paulson, E. J., and Hargus, W. A., "Heat Transfer Measurements in an Elevated Pressure RDRE Combustor," *AIAA Propulsion and Energy Forum, 2021*, 2021, pp. 1–12. https://doi.org/10.2514/6.2021-3685.

[8] Bykovskii, F. A., Zhdan, S. A., and Vedernikov, E. F., "Continuous Spin Detonations," *Journal of Propulsion and Power*, Vol. 22, No. 6, 2006, pp. 1204–1216. https://doi.org/10.2514/1.17656.

[9] Bykovskii, F. A., and Vedernikov, E. F., "Heat fluxes to combustor walls during continuous spin detonation of fuel-air mixtures," *Combustion, Explosion and Shock Waves*, Vol. 45, No. 1, 2009, pp. 70–77. https://doi.org/10.1007/s10573-009-0010-z.

[10] Martinez, A. G., Heister, S. D., Cabot, B., Blong, K., and Teasley, T., "Experimental Study of a Watercooled GOX/RP-1 Rotating Detonation Rocket Combustor for Application to Ox-Rich Staged Combustion Engine Cycles," *AIAA SciTech Forum and Exposition, 2024*, American Institute of Aeronautics and Astronautics Inc, AIAA, 2024. https://doi.org/10.2514/6.2024-2791.

[11] Smallwood, J., "THERMAL AND STRUCTURAL CHARACTERIZATION OF A ROTATING DETONATION ROCKET ENGINE," Ph.D. thesis, Purdue University, 2024.

[12] Hernandez-McCloskey, J., Pineda, D. I., Bennewitz, J. W., Bigler, B. R., Burr, J. R., Danczyk, S. A., Paulson, E. J., and Hargus, W. A., "Design and analysis of an additively manufactured rotating detonation rocket engine chamber for calorimetry and thermal management assessment," *AIAA SCITECH 2023 Forum*, American Institute of Aeronautics and Astronautics, Reston, Virginia, 2023, pp. 1–19. https://doi.org/10.2514/6.2023-0355, URL https://arc.aiaa.org/doi/10.2514/6.2023-0355.

[13] Bartz, D. R., "TURBULENT BOUNDARY-LAYER HEAT TRANSFER FROM RAPIDLY ACCELERATING FLOW OF ROCKET COMBUSTION GASES AND OF HEATED AIR," Tech. rep., Jet Propulsion Laboratory, California Institute of Technology, 1963.

[14] Preclik, D., Wiedmann, D., Oechslein, W., and Kretschmer, J., "Cryogenic rocket calorimeter chamber experiments and heat transfer simulations," *34th AIAA/ASME/SAE/ASEE Joint Propulsion Conference and Exhibit*, American Institute of Aeronautics and Astronautics Inc, AIAA, 1998. https://doi.org/10.2514/6.1998-3440.

[15] Aliakbari, R., Michalski, Q., Mason-Smith, N., Pudsey, A. S., Wenzel, M., and Paull, N., "Heat Flux Measurements of a Methane-Oxygen Rotating Detonation Rocket Engine," *International Workshop on Detonation Propulsion*, Berlin, Germany, 2022. URL https://www.researchgate.net/publication/364221846.

[16] Lienhard IV, J. H., and Leinhard V, J. H., *A Heat Transfer Textbook*, 5th ed., Plogiston Press, Cambridge, MA, 2019.

[17] Sutton G, and Biblarz O, "Rocket Propulsion Elements (9th Edition)," Tech. rep., 2016.

[18] Moran, M. J., Shapiro, H. N., Boettner, D. D., and Bailey, M. B., *Fundamentals of Engineering Thermodynamics*, 7th ed., John Wiley & Sons, Inc., 2010.

[19] Seltzer, S. M., "CCRI(I)/07-17 Recent Dosimetry Activities at the NIST," Tech. rep., 2007.

[20] Tosh, R. E., and Chen-Mayer, H. H., "Frequency-domain characterization of heat conduction in sealed water calorimeters," *Nuclear Instruments and Methods in Physics Research, Section A: Accelerators, Spectrometers, Detectors and Associated Equipment*, Vol. 580, No. 1 SPEC. ISS., 2007, pp. 594–597. https://doi.org/10.1016/j.nima.2007.05.230.

[21] Davids, N., and Berger, R. L., "Simulation Method for the Design and Data Correction of Calorimeters," *Currents in Modern Biology*, Vol. 3, 1969, pp. 169–179.